CrossMark

RESEARCH PAPER

Effects of welding parameters on weld pool characteristics and shape in hybrid laser-TIG welding of AA6082 aluminum alloy: numerical and experimental studies

Amir Hossein Faraji[1] · Massoud Goodarzi[1] · Seyed Hossein Seyedein[1] · Carmine Maletta[2]

Abstract The effects of three important welding parameters including laser power, welding current and welding speed on the weld pool characteristics, shape and dimensions in hybrid laser-TIG welding of AA6082 aluminum alloy are studied by numerical, experimental, and statistical approaches. For this aim, first, a 3D numerical model is used to simulate heat transfer and fluid flow in the weld pool and then resultant weld shape for various welding conditions. Besides, a set of experiments are performed to validate and calibrate the model. Finally, analysis of variance (ANOVA) method is applied to investigate more precisely how welding parameters affect weld dimensions. The simulation results show with increasing the laser power and welding current and decreasing the welding speed, the Marangoni and buoyancy forces increase. With increasing the laser power, the weld depth increases more significantly than the weld width. The weld half width increases with increasing the welding current, whereas the weld pool depth is relatively unchanged. Furthermore, with increasing the welding speed, both weld pool depth and half

width decrease with similar slope. Generally, the presented model showed a good capability to predict the weld geometry and characteristics under various applied welding conditions which can reduce number of needed experiments.

1 Introduction

Hybrid laser-arc welding process is a modern welding process which combines a laser beam and an electric arc to incorporate the advantages of both laser and arc welding processes and overcome their individual problems [1–5]. Hybrid laser-arc welding has attracted particular attention in many areas of industry including automotive, pipeline, aerospace, and shipbuilding industry during recent years [1, 2, 6]. Several advantages have been reported for laser-arc hybrid welding process including better arc stability, more stable laser-generated keyhole, better gap bridging ability compared to laser welding which can reduce joint fitting difficulty and machining costs, and ability for welding with higher speed compared to both lone arc and laser welding [1, 3, 5, 7–9]. In addition, hybrid welding can improve the weld quality with reduced amount of pores and reduced susceptibility to cracking compared to lone laser welding process [3, 7, 10].

The advantages of hybrid laser-arc welding process are because of the interaction and synergy effect between laser and arc sources. Several experimental studies have firmly investigated this synergy effect. They proved that laser-generated metal vapors leaving the keyhole are the main reason of the laser-arc synergy effect. Since the electric arc travels along the path with highest electrical conductivity and metal

✉ Amir Hossein Faraji
   Amirhossein.faraji@gmail.com; a_faraji@iust.ac.ir

   Massoud Goodarzi
   mgoodarzi@iust.ac.ir

   Seyed Hossein Seyedein
   seyedein@iust.ac.ir

   Carmine Maletta
   Carmine.maletta@unical.it

[1]   School of Metallurgy and Materials Engineering, Iran University of Science and Technology, Tehran, Iran

[2]   Department of Mechanical Engineering, University of Calabria, Arcavacata di Rende, Cosenza, Italy

vapors have higher electrical conductivity than shielding gas, the arc tends to bend and root toward the keyhole mouth [3, 11, 12]. In addition, the arc contracts as its effective radius decreases because of increasing the electrical conductivity of plasma caused by the presence of metal vapors [1, 3, 11]. Both these phenomena result in increasing the arc stability and efficiency, peak arc power density, and then melting efficiency [3, 11].

It is worth mentioning that hybrid laser-arc welding involves many process parameters that should be well adjusted to obtain stable process and desired weld size and quality [1, 13, 14]. The most important process parameters of hybrid welding are laser power, welding current, welding speed, arc length, shielding gas, order of laser and arc sources, and relative distance between laser and arc [1, 2, 14]. As a result, studying the effects of these process parameters on resultant weld characteristic seems to be a critical task. Y. B. Chen et al. [11] studied experimentally the effects of welding current, welding speed, and relative distance between laser and arc on the weld pool dimensions in CO_2 laser-TIG hybrid welding of AISI 321 stainless steel plates. Ming Gao et al. [15] studied experimentally the effects of gas shielding parameters including gas composition and velocity on the weld penetration depth dimensions in CO_2 laser-TIG hybrid welding of 316-L stainless steel plates. Giovanni Tani et al. [16] investigated experimentally the effects of gas shielding type and flow rate on the weld depth and width in CO_2 laser–MIG welding of AISI 304 stainless steel plates. L. M. Liu et al. [17] carried out several experiments to study the effects of the laser-TIG order, and relative distance between laser and TIG sources on the weld penetration in Nd:YAG laser-TIG welding on plates of magnesium alloy AZ31B. G. X. Xu et al. [18] studied the effects of laser power and welding speed in laser beam and laser-pulsed GMAW hybrid welding processes for mild steel plates using an adaptive volumetric heat source models. B. Ribic et al. [3] studied experimentally and numerically the effects of welding current, laser power, and relative distance between laser and arc on the weld pool depth and width in Nd:YAG laser/GTAW hybrid welding of A131 structural steel. M. M. Atabaki [19] surveyed the influence of several welding parameters on the weld pool shape for hybrid laser arc welding of aluminum alloys in the thick T-joint configuration using a numerical finite element model.

With respect to large number of process parameters in hybrid laser-arc welding, numerical modeling can be advantageously used to predict weld characteristics, especially the weld pool geometry which significantly affects the weld strength [20, 21], for wide ranges of welding parameters and their combinations. As a result, numerical modeling can result in a remarked reduction of needed experiments for welding optimization, which causes time and money saving. Moreover, numerical modeling can aid for better understanding of how the welding parameters affect the heat transfer and fluid flow in the weld pool. Therefore, mathematical and numerical modeling approaches were used as the effective tools to predict heat transfer and fluid flow, and consequently the weld pool shape and size in recent years [3, 4, 6, 13, 18, 21–24]. However, most studies on hybrid laser-arc welding process are focused on just experimental investigations and a few numerical studies are presented on this process. On other hand, the majority of numerical studies on hybrid welding are concerned with steel alloys and study on hybrid welding of aluminum alloys has received less attention in literatures. It is worth noting that physical properties of aluminum alloys are quite different from those of steel alloys, and therefore, the effects of welding parameters on the weld pool characteristics and shape will be different, and thus, need to be more studied.

Consequently, the main aim of this study is to study the effect of some important welding parameters such as laser power, welding current, and welding speed on the weld pool characteristics and geometry in Nd:YAG laser-TIG hybrid welding of AA6082 aluminum alloy by using an appropriate numerical model. For this purpose, a comprehensive 3D heat transfer and fluid flow model employing a new two-part volumetric laser heat source model and an appropriate 3D electromagnetic model instead of assuming axisymmetric condition like majority of previous studies, is used here. It is worth noting that complete details of this 3D numerical model are presented in our previous work [25], and this work is more focused on developing the model for various welding conditions and then investigating how welding parameters affect heat transfer and fluid flow in the weld pool and weld shape. Besides, several experiments are performed for validation of the presented model and adjusting the heat source parameters for those various welding conditions. Thereafter, several weld pool characteristics including temperature distribution and relative importance of molten pool driving forces, weld dimensions, and weld shape are extracted from the numerical model for those various welding conditions. Finally, an analysis of variance (ANOVA) is carried out to study more accurately how the welding parameters affect the weld pool depth and half width, and also to analyze welding parameter interactions.

2 Mathematical model

To simulate heat transfer and fluid flow and consequently, to predict weld pool characteristics and shape, a comprehensive 3D numerical model is used for various welding conditions. Since this numerical model is described in detail in our previous work [25], we explain the model briefly in this section. Figure 1 illustrates the calculation domain and its boundary surfaces in a 3D Cartesian coordinate system. Due to the symmetry of the weld about the weld center line, only half of the workpiece is used as the calculation domain. The calculation domain dimensions are 40, 15, and 3 mm along x, y, and z
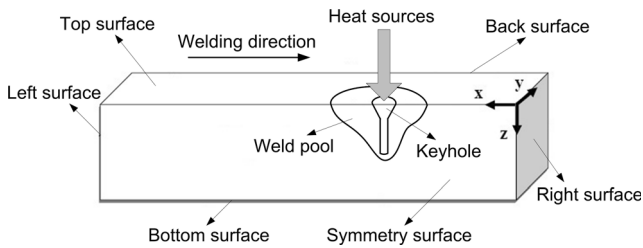
Fig. 1 Calculation domain and boundary surfaces used in the numerical model

directions, respectively. The problem is treated as a steady-state problem by using a coordinate system moving with the welding heat sources [26, 27]. In laser and hybrid welding, keyhole formation has two effects on the weld pool. First, the keyhole dynamic affects the fluid flow, and second, the keyhole changes extremely the heat transfer pattern because the laser heat is entered below the surface by the keyhole [1, 3, 4, 6, 13, 18, 28–30]. Since in hybrid laser-arc welding the keyhole has usually a good stability [1–3, 25, 31, 32] and the keyhole size is so smaller than the weld pool size [3, 18], the first effect has less influence on the weld pool shape than the second one, and as a result, the keyhole dynamic is ignored in some previous studies to simplify modeling and reduce computational time [4, 6, 13, 18, 19, 29, 30, 33, 34]. However, even if the keyhole dynamic is not physically simulated in this study, the main effect of the keyhole, i.e., entering the laser heat into the workpiece via the keyhole has been taken into account by using a new and adaptive two-part volumetric heat source model for the laser source which is calibrated with some experiments.

2.1 Heat transfer and fluid flow in the weld pool

The heat transfer and fluid flow in the weld pool are modeled by solving the conservation equations of mass, momentum, and energy. As well, four equations taken from Maxwell equations are simultaneously solved to attain the distribution of current density and magnetic field and then to calculate the electromagnetic force in the workpiece.

The momentum equation solved for calculation of liquid metal flow can be expressed as follows:

$$\nabla \cdot \left(\rho \overrightarrow{u}\, \overrightarrow{u} \right) = -\nabla p + \nabla \cdot \left(\mu \nabla \overrightarrow{u} \right) + \nabla \cdot \left(\mu \overrightarrow{V_w}\, \overrightarrow{u} \right) + \overrightarrow{S}_u \quad (1)$$

where ρ is the density, $\overrightarrow{u}$ is the fluid velocity vector, p is the pressure, μ is the effective viscosity, $\overrightarrow{V_w}$ is the welding speed vector which is only nonzero along the x direction, and $\overrightarrow{S}_u$ is the vector of source term for momentum equation which is given as follows: $\overrightarrow{S}_u = -C \left(\frac{(1-f_l)^2}{f_l^3 + B} \right) \overrightarrow{u} + \rho \overrightarrow{g} \beta \left(T - T_{ref} \right) + \overrightarrow{F}_{Lorentz}$, where $\overrightarrow{g}$ is the gravitational acceleration vector, β is the thermal expansion coefficient, T is the temperature,

T_{ref} is the reference temperature, C is a constant related to the mushy zone morphology (set to 1.6×10^4 in this study [23, 35–37]), B is a very small constant introduced to avoid division by zero, f_l is the liquid fraction, and $\overrightarrow{F}_{Lorentz}$ is the vector of Lorentz electromagnetic force. In this equation, the first term on the right indicates the frictional forces in the mushy zone based on the Carman-Kozeny equation for flow through a porous media [23, 35, 36], the second and third terms are buoyancy and electromagnetic forces in the weld pool, respectively.

The following mass equation is solved in conjunction with momentum equation to calculate the pressure field.

$$\nabla \cdot \left(\rho \overrightarrow{u} \right) = 0 \qquad (2)$$

The energy equation solved to obtain temperature field in the workpiece is expressed as follows:

$$\nabla \cdot \left(\rho \overrightarrow{u} h \right) = \nabla \cdot \left(\frac{k}{C_p} \nabla h \right) - \nabla \cdot \left(\rho \overrightarrow{V}_w h \right) - \nabla \cdot \left(\rho \overrightarrow{V}_w \Delta H \right) - \nabla \cdot \left(\rho \overrightarrow{u} \Delta H \right) + S_h$$

$$(3)$$

It is worth mentioning that due to the melting phenomena during welding process, the total enthalpy, H, is defined as the sum of sensible heat, h, and latent heat content, ΔH, i.e., $H = h + \Delta H$ [3, 35, 37]. The latent heat can be expressed as $\Delta H = f_l L_f$. For simplicity, the liquid fraction, f_l, is assumed to vary linearly with temperature in the mushy zone as presented in previous studies [20, 21, 25, 35, 38, 39]. S_h is the source term of energy equation which is defined as $S_h = \left| \overrightarrow{J} \right|^2 / \sigma + q_{laser}$, where $\overrightarrow{J}$ is the current density vector, σ is the electrical conductivity, and q_{laser} is the volumetric heat input from the laser source.

Due to the presence of electrical arc in welding, an electromagnetic or Lorentz force is created because of the interaction between the current and the self-induced magnetic field. To calculate the current density vector, current continuity equation, Eq. (4), which is given by Gauss law, is solved.

$$\nabla^2 \varphi = 0 \qquad (4)$$

where φ is the electrical potential. From the calculated electrical potential field, the current density vector is deduced from Ohm's law as $\overrightarrow{J} = -\sigma \nabla \varphi$.

In order to calculate the self-induced magnetic field, potential vector equations need to be solved which can be expressed as follows:

$$\nabla^2 \overrightarrow{A} + \mu_m \overrightarrow{J} = 0 \qquad (5)$$

where $\overrightarrow{A}$ is the potential vector and μ_m is the magnetic permeability ($4\pi \times 10^{-7} N.A^{-2}$). Knowing the potential vector in the computational domain, the self-induced magnetic field can

be obtained as $\overrightarrow{B} = \nabla \overrightarrow{A}$. Eventually, the Lorentz force can be calculated as $\overrightarrow{F}_{Lorentz} = \overrightarrow{J} \times \overrightarrow{B}$.

Besides, a turbulence model based on Prandtl's mixing length hypothesis described in previous studies [3, 23, 25, 37] is applied to calculate effective viscosity and thermal conductivity in the weld pool.

2.2 Heat source model

Defining the distribution of welding heat source is an important step in simulation of the welding process. Due to the completely different nature of the arc and laser heat sources, two different heat source models are used. A surface heat source model is used for TIG source and a volumetric heat source model is used for laser source.

Since heat input from the arc is mainly focused on the top surface [3, 21, 25], it was assumed that heat input and current flux from arc source obey the Gaussian distribution as follows:

$$
\begin{cases}
q_{arc} = \dfrac{\eta_{arc} f_{arc} VI}{\pi R_{arc}^2} \exp\left(-\dfrac{f_{arc} r^2}{R_{arc}^2}\right) \\
J_{arc} = \dfrac{f_{arc} I}{\pi R_{arc}^2} \exp\left(-\dfrac{f_{arc} r^2}{R_{arc}^2}\right)
\end{cases}
\tag{6}
$$

where q_{arc} is the arc heat input, J_{arc} is the welding current flux, η_{arc} is the arc efficiency, f_{arc} is the arc distribution parameter, V is the arc voltage, I is the welding current, R_{arc} is the effective arc radius, and r is the radial distance to the arc root which is given as $r = \sqrt{(x-x_0)^2 + y^2}$. x_0 is the x-position of the arc root.

In hybrid welding, a cavity containing ionized vapors, keyhole, is created because of the high laser intensity and, as a result, the laser energy can be transferred below the workpiece surface [3, 11, 40, 41]. Corresponding to the reversed-bugle shape of the keyhole predicted in some previous literatures [40–43], a combined heat source model is applied for laser heat in this study. As schematically shown in Fig. 2, this heat source model consists of a conical volumetric source in the upper part ($0 < z < z_i$) and a cylindrical volumetric source in the lower part ($z_i < z < z_{keyhole}$) which is expressed as

$$
q_{laser} = \begin{cases}
\dfrac{\chi_{upper} \eta_{laser} f_{laser}^2 P}{\pi (1-e^{-3})(z_i)\left(r_i^2 + r_i.r_e + r_e^2\right)} \exp\left(-\dfrac{f_{laser} r^2}{R_{laser}^2}\right); & for \ 0 < z < z_i \\
\dfrac{(1-\chi_{upper}) \eta_{laser} P}{\pi r_i^2 (z_{keyhole} - z_i)}; & for \ z_i < z < z_{keyhole}
\end{cases}
\tag{7}
$$

where q_{laser} is the volumetric laser heat input, χ_{upper} is the upper laser energy contribution, η_{laser} is the laser efficiency, f_{laser} is the laser distribution parameter, P is the laser power, z_i is the z-coordinate of cone end, $z_{keyhole}$ is the keyhole depth, and r_e and r_i are the radii of cone ends. R_{laser} is the effective
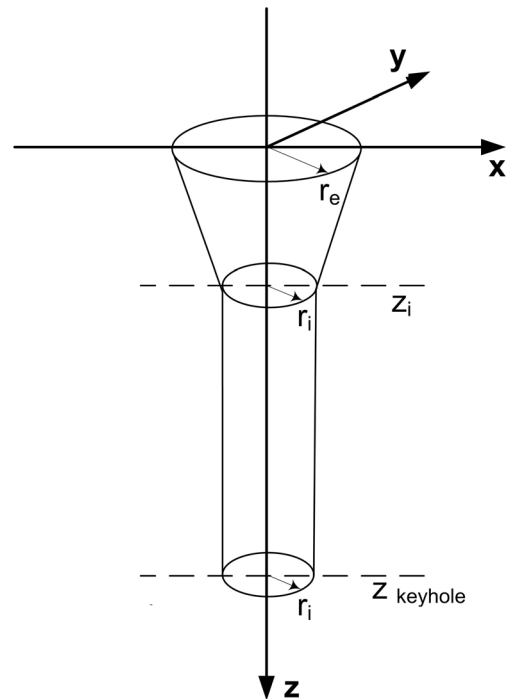

Fig. 2 Schematic presentation of volumetric model of the laser heat source used in the modeling

laser radius at upper part which is given as $R_{laser} = r_i + \frac{(r_i - r_e)}{z_i}.(z-z_i)$, r is the radial distance to the laser focal point which is given as $r = \sqrt{(x-x_0)^2 + y^2}$, and x_0 is x-position of the laser focal point.

2.3 Boundary conditions

The boundary conditions used in the present model are discussed in detail as follows:

Top surface

At the top surface, Marangoni surface tension arisen from temperature gradient of surface tension coefficient is applied for momentum equation which is given as $\overrightarrow{\tau_{st}} = f_l \frac{d\gamma}{dT} \frac{\partial T}{\partial s}$, where $\overrightarrow{s}$ and $\frac{d\gamma}{dT}$ are the local tangent vectors to the top free surface and the temperature coefficient of surface tension, respectively. For energy equation, arc heat input minus convective and radiation heat loss, i.e., $q = q_{arc} - h_f(T-T_a) - \sigma_{Boltz.}\varepsilon(T^4 - T_a^4)$, is applied, where h_f is the heat transfer coefficient, $\sigma_{Boltz.}$ is the Stefan-Boltzman constant, ε is the surface emissivity, and T_a is the ambient temperature. For the potential equation, welding current flux is applied at the top surface.

Symmetry surface

Symmetric boundary condition, i.e., zero flux across the surface, is applied for all dependent variables.

Bottom surface

At the bottom surface, because only partial weld penetration is considered here, and thus the weld pool does not extend to the bottom, all velocities are zero. Furthermore, the heat loss by convection and radiation is used for energy equation. For the potential equation, electrical potential gradient is set to zero at the bottom surface.

Other surfaces

At other surfaces far away from the heat sources, the temperature is set to ambient temperature and the velocities are zero. For the potential equation, electrical potential is set to zero at all of these surfaces.

In addition, for potential vector equations, zero gradients are used for all boundaries.

2.4 Modeling approach

The governing equations are solved by using the FLUENT software which is based on finite volume method (FVM). Particular abilities of FLUENT to add C++ programming codes by user-defined function (UDF) and to add extra scalar equations by user-defined scalar (UDS) are used, in order to enhance the FLUENT code for solving added equations for electromagnetic model, computing the current density, magnetic field, and electromagnetic force and also handling source terms and boundary conditions. To improve computation efficiency, a nonuniform grid system with finer grids near the heat source location is employed. Furthermore, the material properties used to complete the mathematical modeling are listed in Table 1.

3 Experimental procedure

In order to calibrate and validate the numerical model, some experiments are carried out. AA6082 aluminum alloy plates

Table 1 Material properties used in mathematical model

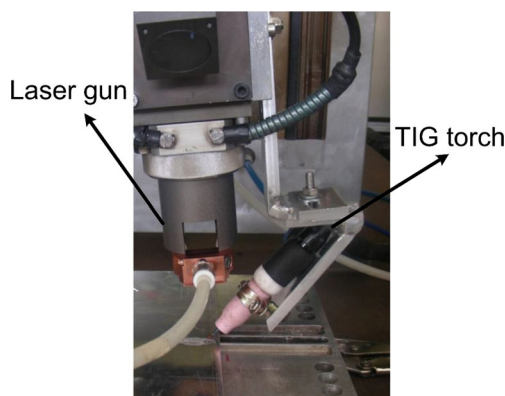| Property	Symbol	Unit	Value
Density	ρ	kg/m^3	2700
Viscosity	μ	kg/m/s	0.001
Thermal conductivity	k	W/m/K	$\begin{cases} 220 & , T \leq 923 \\ 150 & , T > 923 \end{cases}$
Specific heat	C_p	J/kg/K	$\begin{cases} 900 & , T \leq 923 \\ 1200 & , T > 923 \end{cases}$
Latent heat of fusion	L_f	J/kg	395000
Thermal expansion	β	/K	2.3×10^{-5}
Liquidus temperature	T_l	K	923
Solidus temperature	T_s	K	858
Electrical conductivity	σ	A/V/m	3.12×10^7

Fig. 3 Experimental setup of hybrid laser-TIG welding process

with the thickness of 3 mm are used in this work. Hybrid linear bead-on-plate welds were made on the plates, using a Nd:YAG laser with maximum power of 2000 W, accompanied by a TIG welder with maximum welding current of 350 A. laser-leading configuration as shown in Fig. 3 is used
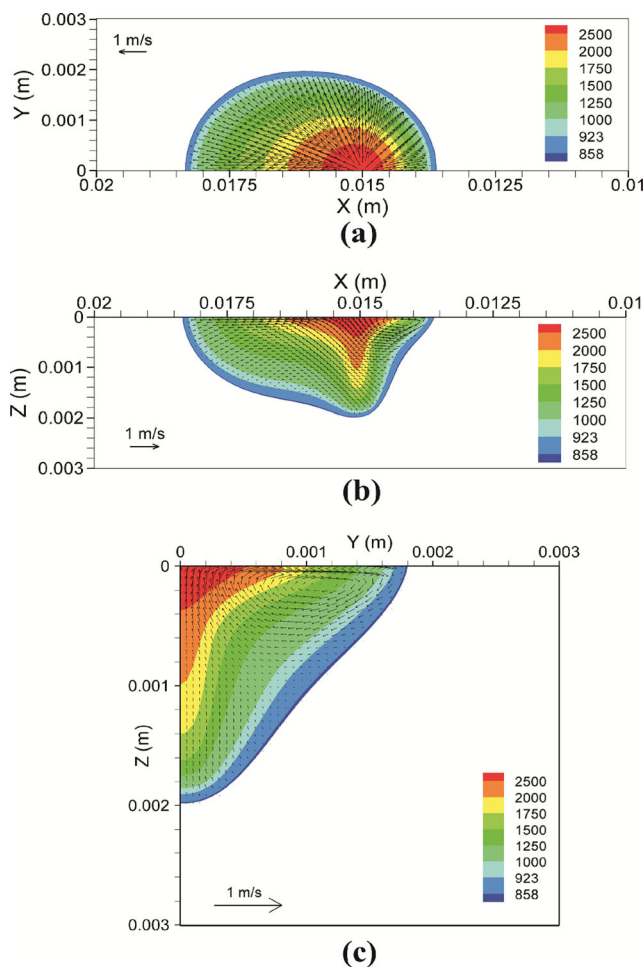

Fig. 4 Temperature contours and velocity field in the weld pool (**a**) at the top surface, (**b**) in the longitudinal section, and (**c**) at the weld cross section for P=2000 W, I=100 A, and V_w=2000 mm/min

here. The arc-to-laser distance and arc length are set to 0 and 2 mm, respectively. These values are chosen based on some preliminary welding tests. The arc voltage is about 15 V for a 100-A arc and 16 V for a 150-A arc. Spot diameter of the laser beam on the workpiece surface is about 0.5 mm. Argon is used as the shielding gas. The inclination angle of the TIG torch and laser beam are 5° and 30°, respectively, so that both the laser spot and arc root are located at the same point.

Two levels are used for every welding parameter including the laser power, welding current, and welding speed. The laser power levels are 1000 and 2000 W, the welding current levels are 100 and 150 A, and the welding speed levels are 2000 and 3000 mm/min.

Before welding, each sample was mechanically polished and then degreased with acetone, to remove oxides and other residues. After welding, in order to compare the numerical predictions and experiments, the shape and dimensions of
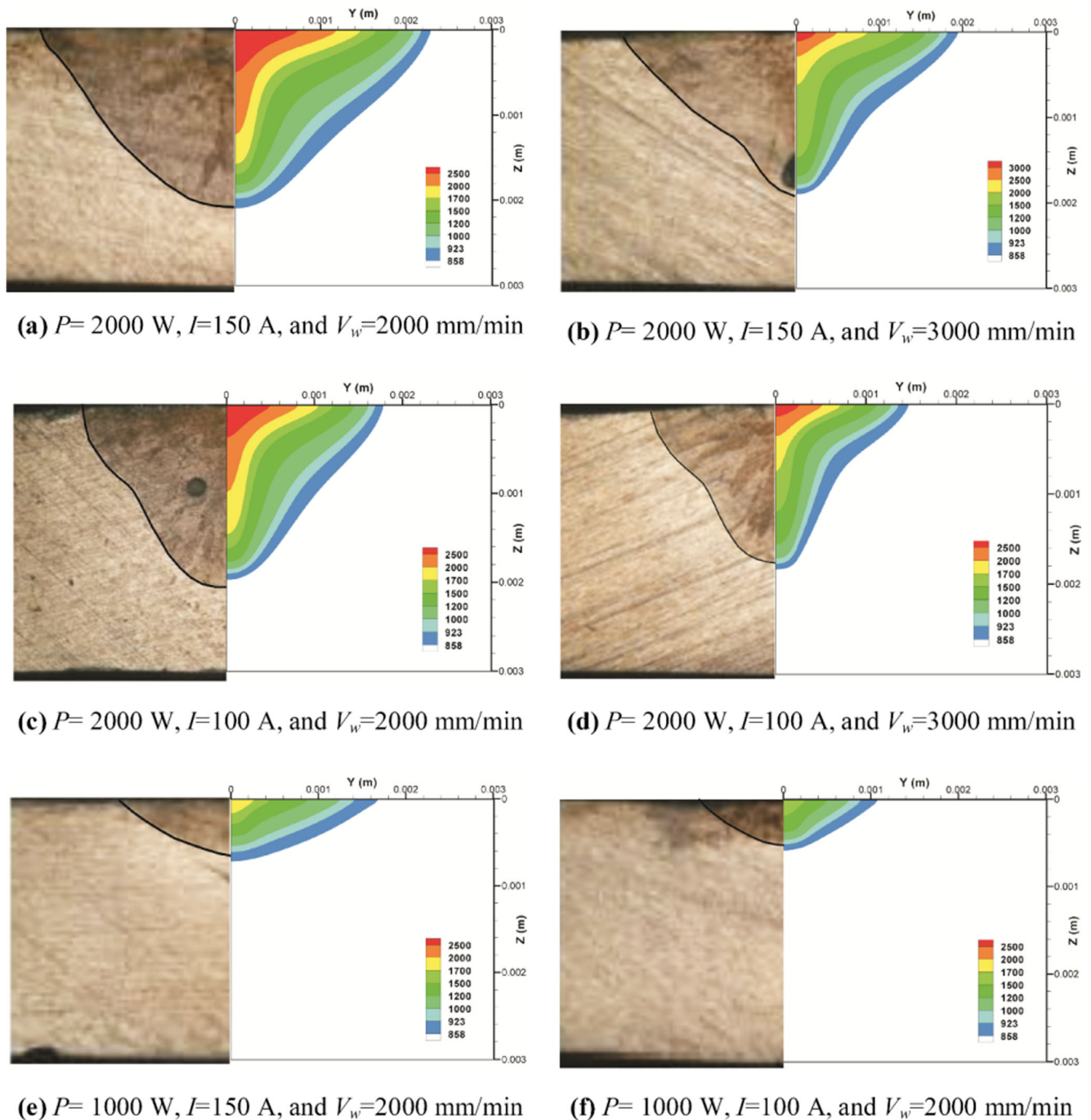

(a) $P= 2000$ W, $I=150$ A, and $V_w=2000$ mm/min

(b) $P= 2000$ W, $I=150$ A, and $V_w=3000$ mm/min

(c) $P= 2000$ W, $I=100$ A, and $V_w=2000$ mm/min

(d) $P= 2000$ W, $I=100$ A, and $V_w=3000$ mm/min

(e) $P= 1000$ W, $I=150$ A, and $V_w=2000$ mm/min

(f) $P= 1000$ W, $I=100$ A, and $V_w=2000$ mm/min

Fig. 5 Comparison between simulated and experimental weld cross section in hybrid welding for various welding conditions

the weld bead were measured by optic microscopic observations. Therefore, all samples were sectioned from the middle of the weld line and then mounted, polished, and etched to attain the cross-sectional shape of the weld bead.

4 Results and discussion

4.1 Adjusting heat source parameters

The adjustment of heat source parameters plays an important role in numerical modeling of the welding process, i.e., the physical and phenomenological parameters used in Eq. (6) for the arc source and in Eq. (7) for the laser source.

Arc heat source parameters are η_{arc}, f_{arc}, and R_{arc}. f_{arc} is assumed to be 2 based on some previous studies [26, 27, 44]. Because of high arc stability in hybrid welding process, η_{arc} is assumed to be 80 %. Therefore, the only parameter needed to be adjusted in arc heat source model is the effective arc radius (R_{arc}).

Laser heat source parameters are η_{laser}, f_{laser}, χ_{upper}, R_i, R_e, Z_i, and $Z_{keyhole}$. Due to highly focused laser beam and high laser energy absorption because of multiple reflections in the keyhole [3, 45], f_{laser} and η_{laser} are set to 3 and 85 %, respectively. According to calculated keyhole shapes reported in the previous literatures [40, 46], the z-coordinate of cone end and radius of cone ends were assumed as $R_i=R_{laser}$, $R_e=2R_{laser}$, and $Z_i=0.25Z_{keyhole}$. As well, the upper laser energy factor is set to 0.5. Therefore, the only parameter needed to be adjusted in laser heat source model is the keyhole depth ($Z_{keyhole}$).

In addition, since the interaction between the arc and laser in hybrid welding causes the arc to bend toward the keyhole [3, 47], the laser focal point and the arc root are considered to be positioned at the same location, i.e., we set $x_0=15$ mm in both laser and arc heat source equations.

Based on the above explanations, the heat source model for hybrid welding process has only two adjustable parameters,
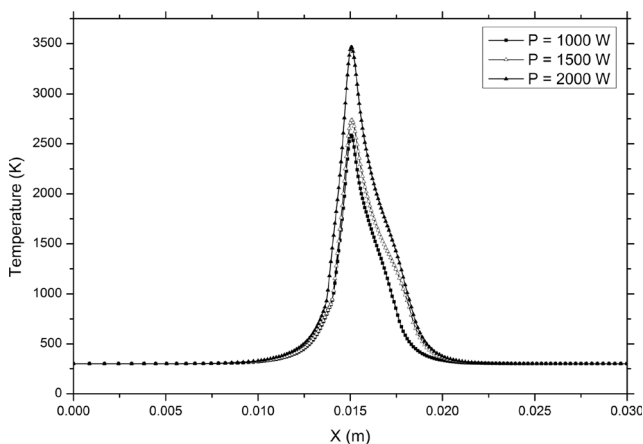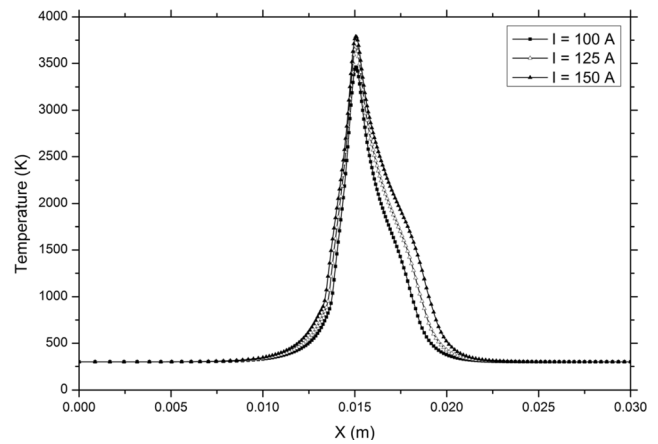

Fig. 7 Variations of the temperature along x direction in different levels of welding current for P=2000 W and V_w=2000 mm/min

i.e., R_{arc} and $Z_{keyhole}$, which are defined by comparing the simulated and experimental weld pool shapes to obtain a good match. It is worth noting that R_{arc} is defined as a function of welding current and $Z_{keyhole}$ is defined as a function of laser power. Accordingly, R_{arc} is defined to be 1.5 mm for 100-A arc and 2 mm for 150-A arc, and $Z_{keyhole}$ is defined to be 0.4 for 1000-W laser and 1.8 mm for 2000-W laser. For the range between these welding parameters, R_{arc} and $Z_{keyhole}$ are defined by linear interpolation approach.

It is important to mention that the arc effective radius values calculated here in hybrid laser-TIG welding process are lower than those in lone TIG welding process reported in previous studies [48, 49]. This outcome shows the fact that the arc in hybrid laser-TIG welding is constricted because of the laser-arc interaction which is in agreement with previous literatures [1–3, 31, 50].

4.2 Simulated temperature and velocity fields

Figure 4 presents temperature and velocity distributions at the top surface (a), longitudinal (b), and cross section (c) of the
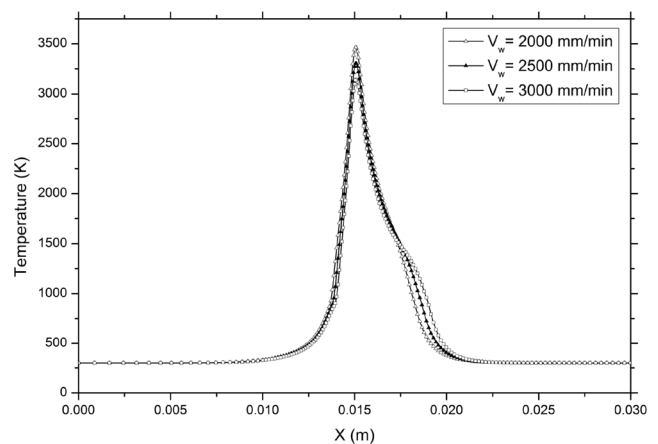

Fig. 6 Variations of the temperature along x direction in different levels of laser power for I=100 A and V_w=2000 mm/min

Fig. 8 Variations of the temperature along x direction in different levels of welding speed for P=2000 W and I=100 A

Table 2 Weld pool characteristics and dimensionless numbers as function of welding parameters

	P=1000 W				P=2000 W			
	I=100 A		I=150 A		I=100 A		I=150 A	
	V_w=2000 mm/min	V_w=3000 mm/min	V_w=2000 mm/min	V_w=3000 mm/min	V_w=2000 mm/min	V_w=3000 mm/min	V_w=2000 mm/min	V_w=3000 mm/min
T_{max}(K)	2585	2336	2924	2592	3492	2970	3790	3414
$\left|\vec{V}\right|_{max}$ (m/s)	0.551	0.642	0.544	0.635	0.612	0.723	0.595	0.656
Pe	12.8	13.9	19.7	20.6	23.8	23	29.3	27.5
Gr	55.8	38	251.5	150.2	394.4	172.2	892.2	479.1
Rm	8.6×10^5	8.6×10^5	1.9×10^6	1.9×10^6	8.6×10^5	8.6×10^5	1.9×10^6	1.9×10^6
Ma	7.5×10^5	5.9×10^5	1.4×10^6	1.0×10^6	1.9×10^6	1.2×10^6	2.7×10^6	2.0×10^6

weld pool for the laser power of 2000 W, the welding current of 100 A, and the welding speed of 2000 mm/min. As shown in Fig. 4a, the molten liquid at the top surface of the weld pool flows outward to the solid-liquid interface. As well, it can be observed from Fig. 4c that there is a clockwise vortex of molten material near the top surface. Both of these phenomena approve the presence of a strong Marangoni force in the weld pool.

4.3 Comparing numerical and experimental weld shape

To validate the proposed model and calibrate the heat source model, several comparisons between the experimental weld pool shapes and simulated ones are done. Figure 5 shows the comparisons between the experimental and numerical cross section of the weld pool for various welding conditions. Average difference percentages between simulated and experimental

weld pool depth and half width are 5.9 and 9.6 %, respectively. It is worth mentioning that one of the main sources of these errors may be the assumption of ignoring the keyhole dynamic. However, these low values of average difference percentages, as well as proper match between the simulated and experimental overall weld pool shape for almost all cases, indicate that there is a good agreement between simulation and experiment. This fact proves that presented numerical model can be used as a capable tool to predict the weld pool shape and dimensions under various applied welding conditions.

4.4 Effects of welding parameters on temperature distribution

Figure 6 shows variation of the temperature along x-axis for different laser powers. As seen, the temperature is increased
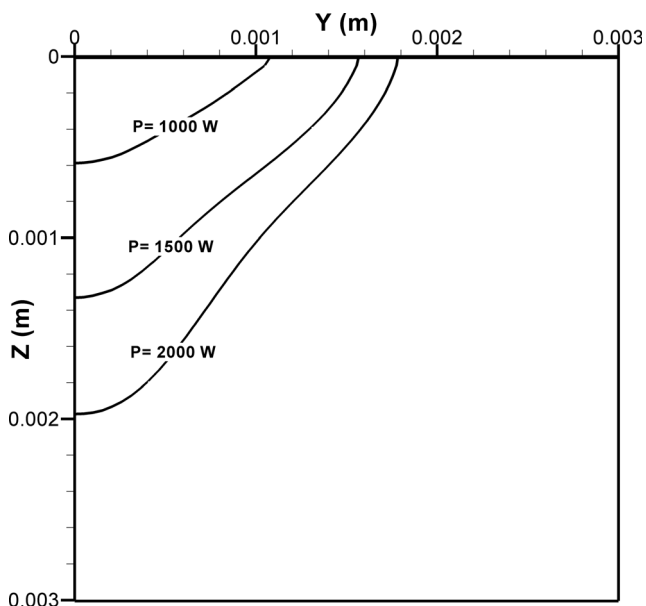

Fig. 9 Weld pool cross-sectional geometry as function of the laser power for a welding speed of 2000 mm/min and welding current of 100 A
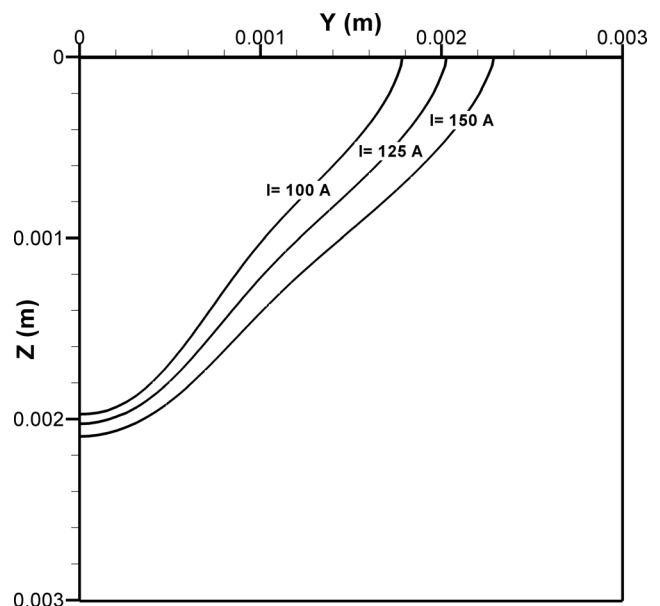

Fig. 10 Weld pool cross-sectional geometry as function of the welding current for a welding speed of 2000 mm/min and laser power of 2000 W
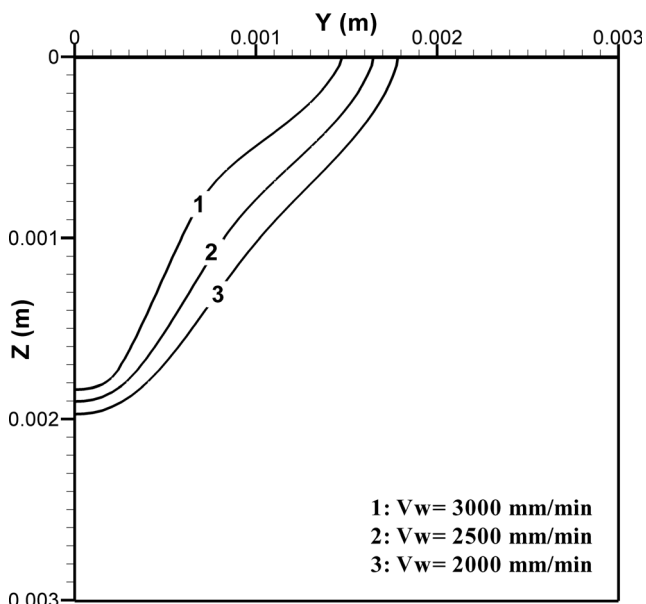
Fig. 11 Weld pool cross-sectional geometry as function of the welding speed for a laser power of 2000 W and welding current of 100 A

and widened by increasing the laser power. The reason is that with increasing the laser power, more heat is entered to the keyhole which causes an increase in temperature. In addition, with increasing the laser power, the weld pool length increases which make the temperature distribution wider. In Fig. 7, the distribution of temperature along x-axis for different welding current values is shown. As clearly observed, the temperature is slightly increased with an increase in welding current; furthermore, the distribution of temperature becomes wider in higher values of welding current. This fact is because of increasing the weld pool length with the welding current which causes a wider distribution of temperature along the x-axis. Figure 8 shows variation of the temperature along x-axis for different welding speeds. As seen, with increasing the welding speed, the temperature becomes lower and its distribution becomes a bit wider which means that the temperature gradient is decreased. In other words, with increasing the welding speed, although net heat input per unit length decreases, the weld pool is elongated which is due to high thermal conductivity of aluminum alloy and consequently the thermal gradient is decreased. This feature is also reported by R. Ray et al. for keyhole mode laser welding of AA5754 aluminum alloy [35]. Figures 6, 7, and 8 represent that changing of temperature is more sensitive to laser power than welding current and

Table 3 Welding parameters with design levels used for statistical investigation

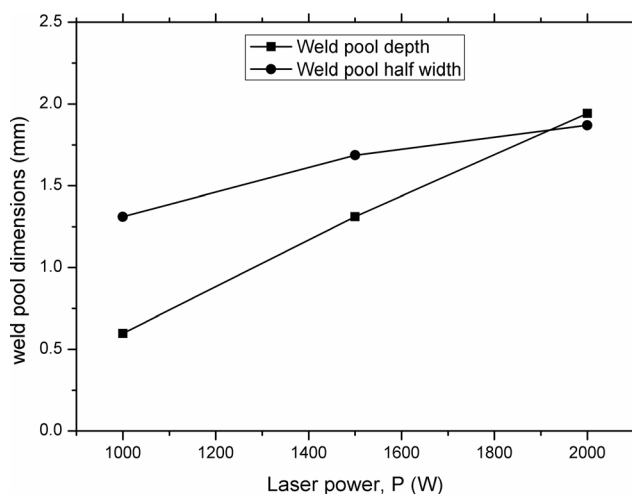| Parameter	Notation	Unit	Level 1	Level 2	Level 3
Laser power	P	(W)	1000	1500	2000
welding current	I	(A)	100	125	150
Welding speed	V_W	(mm/min)	2000	2500	3000

Fig. 12 Effect of the laser power on the overall mean of the weld pool depth and half width

welding speed. In addition, as seen in Figs. 6, 7, and 8, the temperature in keyhole region is high, even higher than the boiling temperature of material for some welding conditions. In fact, the keyhole is filled with high temperature ionized metal vapors named metallic plasma [1–3, 31]. Since the plasma phase in the keyhole is not considered in presented model, high focused laser energy can cause an intense increase in the temperature even higher than the boiling temperature of material in the keyhole region of the workpiece.

4.5 Effects of welding parameters on the weld pool characteristics

Table 2 indicates the effects of welding parameters including laser power, welding current, and welding speed on calculated maximum temperature and liquid velocity experienced in the weld pool. Besides, to investigate the effects of the welding parameters on the heat transfer and fluid flow driving forces in
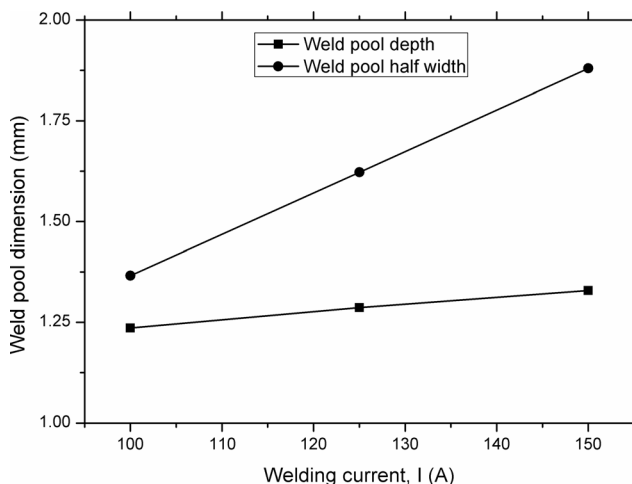

Fig. 13 Effect of the welding current on the overall mean of the weld pool depth and half width
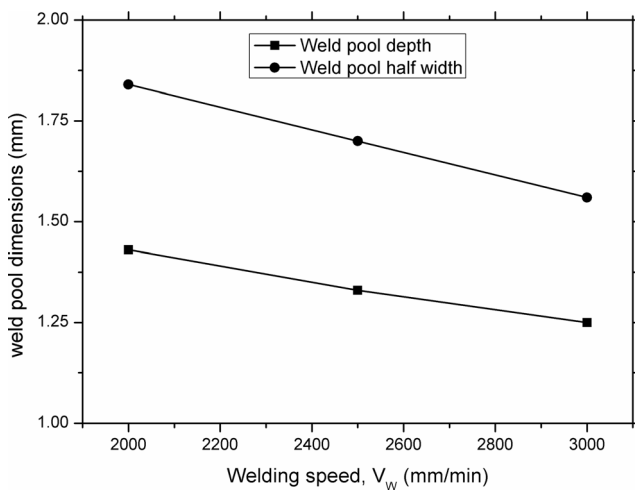
Fig. 14 Effect of the welding speed on the overall mean of the weld pool depth and half width

the weld pool, several dimensionless numbers, such as the Peclet number (Pe), the Grashof number (Gr), the magnetic Reynolds number (Rm), and the surface tension Reynolds number (Ma) are also listed in Table 2. Formulas for calculation of these dimensionless numbers are presented in previous literatures [3, 23, 25, 51]. From Table 2, it is observed that the maximum temperature increases with increase in the laser power and welding current and decrease in welding speed, due to higher heat input from welding sources. It is also seen that the maximum liquid velocity increases by increasing the laser power and welding speed, and decreases by increasing the welding current which is probably due to stronger inward electromagnetic force against outward Marangoni force.

As seen, the calculated Peclet numbers for all cases are much greater than 1 and it means that the fluid flow in the weld pool has a significant effect on the weld pool shape. In addition, regarding the values of Gr, Rm, and Ma, it may be declared that the fluid flow is mainly driven by the Marangoni and electromagnetic forces rather than the buoyancy force.
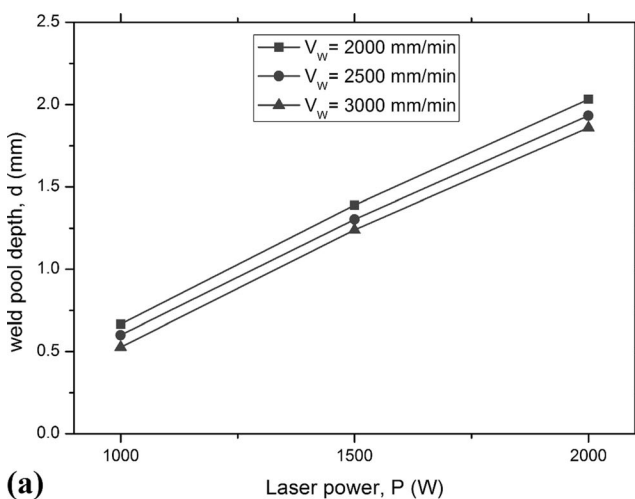
Furthermore, with increasing the laser power and welding current and also decreasing the welding speed, the Marangoni and buoyancy forces increase due to higher temperatures experienced in the weld pool. The electromagnetic force increases only by increasing the welding current, as expected.

4.6 Effects of welding parameters on the weld pool shape

Figure 9 shows the effect of laser power on the cross-sectional weld pool shape. As seen, the laser power has an intense effect on the weld pool shape as with increasing the laser power both the weld depth and half width increase severely. Figure 10 presents the effect of welding current on the cross-sectional weld pool shape. As shown, with increasing the welding current, half width of the weld pool increases significantly, whereas the weld depth increases a little so that is relatively unchanged. Figure 11 shows effect of the welding speed on the cross-sectional weld pool shape. As seen, the weld pool depth and half width increase with decreasing the welding speed. From Figs. 9, 10, and 11, it is found that the effect of laser power on the cross-sectional weld pool shape is more significant compared to other welding parameters, i.e., welding current and welding speed.

4.7 Statistical investigation

After developing numerical model and verifying this model by experiments, a statistical investigation is carried out to study more precisely how the welding parameters affect the weld pool dimensions, including the weld pool depth and half width, and also to analyze welding parameter interactions. For this aim, three levels are considered for every three welding parameters including laser power, welding current, and welding speed as listed in Table 3. A full factorial design of

(a)
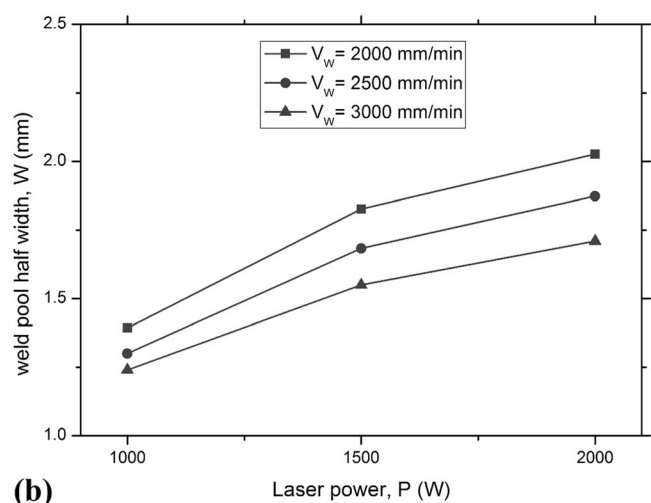
(b)

Fig. 15 Effect of the laser power in different welding speeds on the mean of the **a** weld pool depth and **b** half width
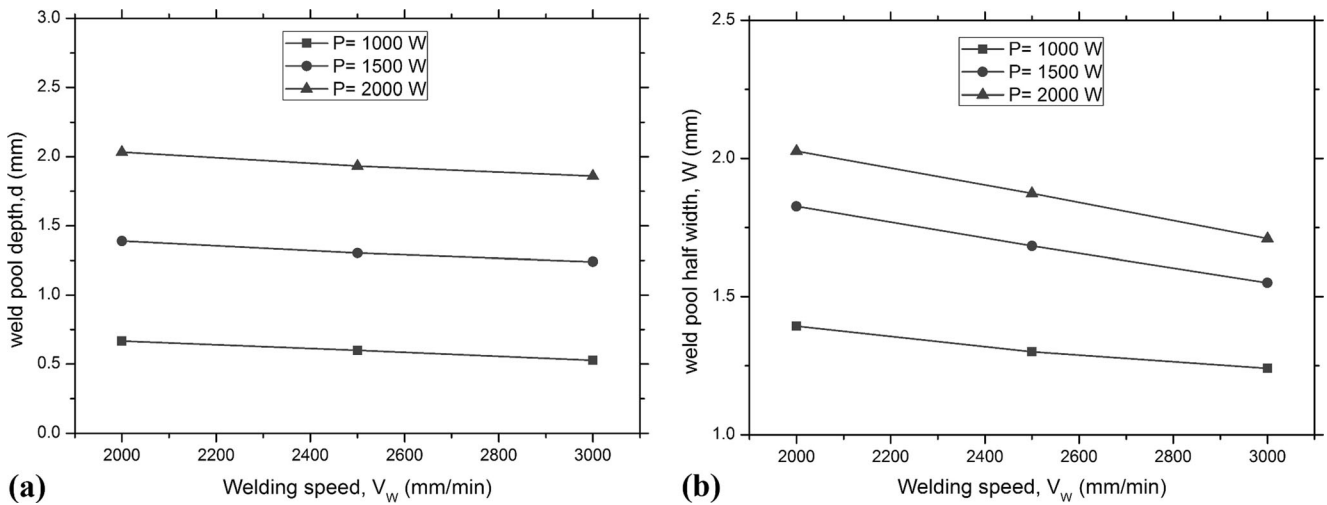
Fig. 16 Effect of the welding speed in different laser powers on the mean of the **a** weld pool depth and **b** half width

these welding parameters, i.e., 27 sets of welding conditions is considered.

Firstly, the validated numerical model is used to predict the weld pool shape and dimensions under all welding conditions. Thereafter, the weld pool depth and half width are taken from the model and then are analyzed by approach of ANOVA. Finally, regression analyses are performed to extract proper equations for weld pool dimensions as a function of welding parameters and their interactions.

4.7.1 Effect of welding parameters on weld pool dimensions

Figure 12 shows the effect of laser power on the overall mean of the weld pool depth and half width. As seen, with increasing the laser power from 1000 to 2000 W, the mean of weld pool depth increases from 0.6 to 1.9 mm and the mean of weld pool half width increases from 1.3 to 1.8 mm. In fact, both weld depth and half width increase by increasing the laser power. However, variation slope for weld depth is noticeably

steeper than that for the weld half width, which can confirm the fact that heat input from laser source is more transferred to workpiece depth via the keyhole.

Figure 13 shows the effect of the welding current on the overall mean of the weld pool depth and half width. As seen, with increasing the welding current from 100 to 150 A, the mean of weld pool depth increases from 1.2 to 1.3 mm and the mean of weld pool half width increases from 1.4 to 1.9 mm. In fact, both weld depth and half width increase with increasing the welding current. However, variation slope for weld half width is remarkably steeper than that for the weld depth which can prove the fact that heat input from arc source is more concentrated on the weld surface than penetrating into the depth.

Figure 14 shows the effect of the welding speed on the overall mean of the weld pool depth and half width. As seen, with increasing the welding speed from 2000 to 3000 mm/min, the mean of weld pool depth decreases from 1.4 to 1.25 mm and the mean of weld pool half width decreases from
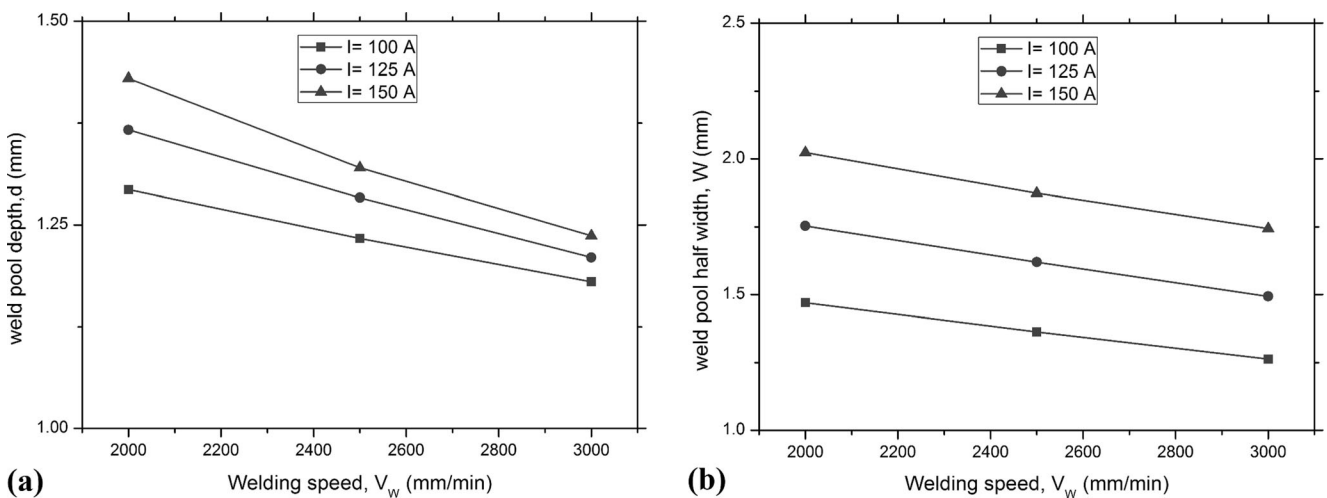

Fig. 17 Effect of the welding speed in different welding currents on the mean of the **a** weld pool depth and **b** half width
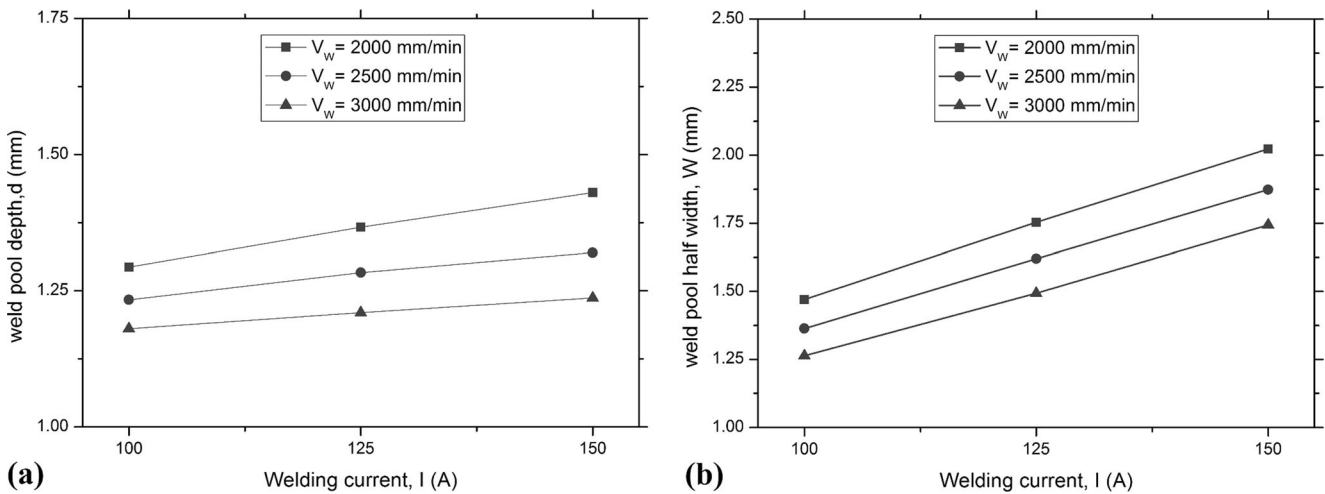
Fig. 18 Effect of the welding current in different welding speeds on the mean of the **a** weld pool depth and **b** half width

1.8 to 1.6 mm. In fact, both weld depth and half width decrease by increasing the welding speed. In addition, variation slopes for weld depth and half width are approximately the same which is due to simultaneous reduction of both laser and arc net heat input per unit length with increasing the welding speed.

Figures 15 and 16 represent the interaction effects between the laser power and welding speed on the weld pool depth and half width. As seen, plot lines of the weld pool depth (Figs. 15a and 16a) are almost parallel while plot lines of the weld half width (Figs. 15b and 16b) are piecewise linear and not parallel. Based on this qualitative observation, it can be stated that there is a higher interaction effect between laser power and welding speed on the weld pool half width than the weld pool depth.

Figures 17 and 18 show the interaction effects between the welding current and welding speed on the weld pool depth and half width. The trends illustrated in Figs. 17a and 18a indicate

an interaction effects between the two welding parameters on the weld pool depth as the lines are not parallel. From Figs. 17b and 18b, similar trend is seen for the weld pool half width, but in this case, a lower interaction effect is expected.

Figures 19 and 20 indicate the interaction effects between the laser power and welding current on the weld pool depth and half width. As seen, the slopes of plot lines are relatively equal in both graphs of weld pool depth and half width. This fact implies that the interaction effects between welding current and welding speed is not so significant.

4.7.2 Analysis of variance and regression

In this section, for a deeper understanding of the results presented in the previous section, an analysis of variance based on the factorial design in Table 3 is conducted. Process responses are the weld pool depth and half width. The results of analysis of variance for the weld pool depth are reported in
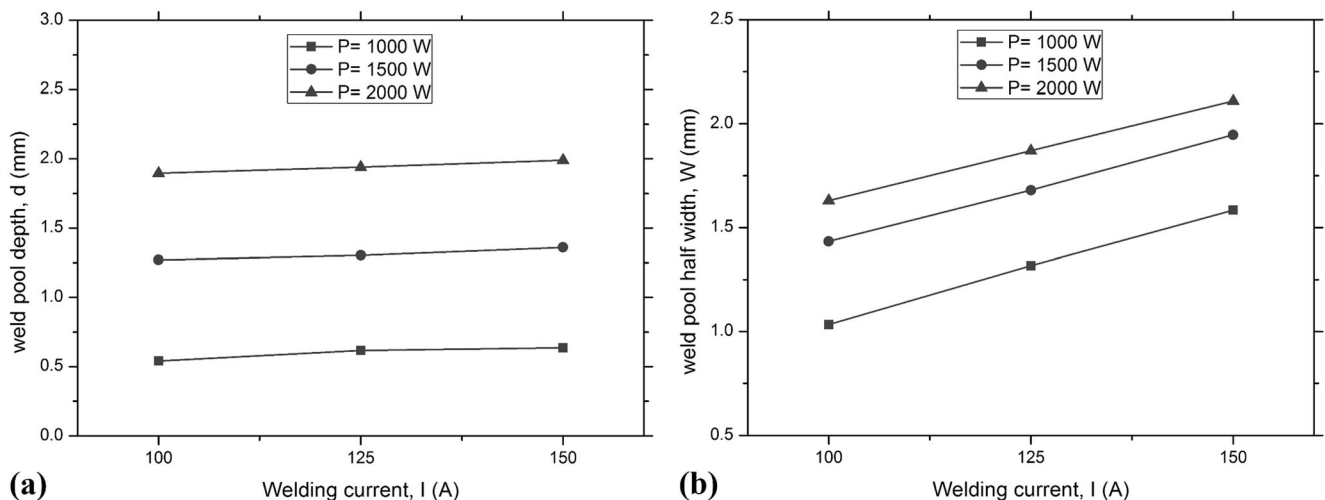

Fig. 19 Effect of the welding current in different laser powers on the mean of the **a** weld pool depth and **b** half width
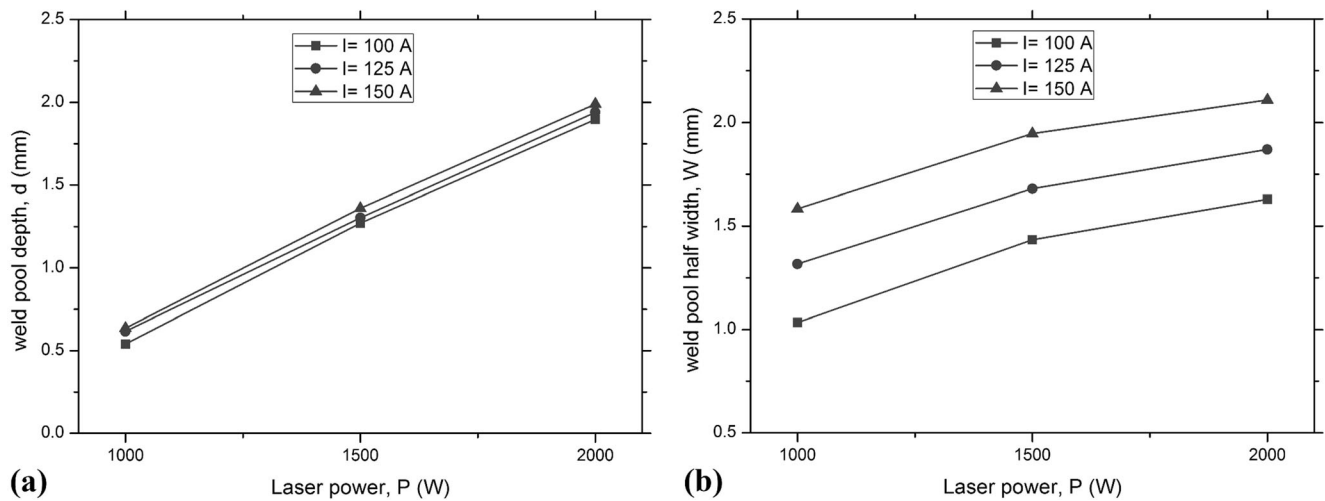
Fig. 20 Effect of the laser power in different welding currents on the mean of the **a** weld pool depth and **b** half width

Table 4, where only the significant sources of variations are reported. As seen, laser power (P) is the most effective parameter. Among quadratic terms, quadratic effect of the laser power ($P \times P$) and also quadratic effect of the welding speed ($V_W \times V_W$) are significant. Likewise, interaction effects between the laser power and welding speed ($P \times V_W$) and also between the welding current and welding speed ($I \times V_W$) are to be considered significant. However, $I \times V_W$ interaction effect is more important than $P \times V_W$ one due to its higher F value. Finally, according to this analysis, the final regression equation of the weld pool depth in terms of welding parameter values yields Eq. (8).

$$
\begin{aligned}
\text{Weld pool depth } = & -1.35317 + 1.86771\,e{-}3\,P \\
& + 0.35333\,e{-}3\,I - 1.64444\,e{-}7\,P \times P \\
& - 1.49667\,e{-}8\,P \times V_W \\
& - 7.43333\,e{-}7\,I \times V_W \\
& + 9.48889\,e{-}9\,V_W \times V_W
\end{aligned}
\tag{8}
$$

The results of analysis of variance for the weld pool half width are reported in Table 5. As observed, laser power (P) and welding current (I) are the most effective parameters. Among quadratic terms, only quadratic effect of the laser power ($P \times P$) is significant. Similarly to the weld pool depth, among the interaction effects, the $P \times V_W$ and $I \times V_W$ interaction effects are to be considered significant. However, $P \times V_W$ interaction effect is more important than $I \times V_W$ one. Eventually, the final regression equation of the weld pool half width in terms of welding parameter values is presented in Eq. (9).

$$
\begin{aligned}
\text{Weld pool half width} = & -1.48222 + 1.87556\,e{-}3\,P \\
& + 1.17556\,e{-}2\,I + 8.97222\,e{-}5\,V_W \\
& - 3.84444\,e{-}7\,P \times P - 8.16667\,e{-}8\,P \\
& \times V_W - 7.33333\,e{-}7\,I \times V_W
\end{aligned}
\tag{9}
$$

Table 4 Analysis of variance and regression of the weld pool depth

Source of variation	Sum of squares	Degree of freedom	Mean squares	F value	P value
Regression	8.29645	6	1.38274	9951.2	0.000000
P	8.13389	1	8.13389	58,537.5	0.000000
I	0.03920	1	0.03920	282.1	0.000000
$P \times P$	0.01014	1	0.01014	73.0	0.000000
$V_W \times V_W$	0.10352	1	0.10352	745.0	0.000000
$P \times V_W$	0.00307	1	0.00307	22.1	0.000136
$I \times V_W$	0.00663	1	0.00663	47.7	0.000001
Error	0.00278	20	0.00014		
Total	8.29923	26			

R-sq=99.97 %, R-sq (pred)=99.94 %

Table 5 Analysis of variance and regression of the weld pool half width

Source of variation	Sum of squares	Degree of freedom	Mean squares	F value	P value
Regression	2.95477	6	0.49246	1076.09	0.000000
P	1.40561	1	1.40561	3071.43	0.000000
I	1.19094	1	1.19094	2602.36	0.000000
V_W	0.27876	1	0.27876	609.12	0.000000
$P \times P$	0.05542	1	0.05542	121.11	0.000000
$P \times V_W$	0.02001	1	0.02001	43.72	0.000002
$I \times V_W$	0.00403	1	0.00403	8.81	0.007591
Error	0.00915	20	0.00046		
Total	2.96392	26			

R-sq=99.69 %, R-sq (pred)=99.34 %

5 Conclusion

The major aim of this work is to investigate how welding parameters including the laser power, welding current, and welding speed affect the weld pool characteristics, shape, and dimensions in hybrid laser-GTA welding of AA6082 aluminum alloy plates. This work can be divided into three parts. In the first part, a three-dimensional numerical model for heat transfer and fluid flow is used for a various ranges of welding conditions. To simplify the model and reduce computational time, the keyhole dynamic is ignored and instead, a new equivalent tow-part volumetric heat source model is introduced for laser source. In the second part, several experiments are performed to validate the numerical model and adjusting the heat source parameters. In the third part, an ANOVA is done on the obtained numerical results to study more precisely the effect of welding parameters and their quadratic and interaction effects on the weld pool depth and half width. The final regression equations in terms of the values of effective parameters are also presented for both weld pool depth and half width. The major conclusions taken from these investigations can be summarized as follows:

1. The results show that with increasing the welding speed, the temperature becomes lower and its distribution becomes a bit wider which is because the weld pool is elongated due to high thermal conductivity of aluminum alloy.
2. By increasing the laser power and welding current, and decreasing the welding speed, both the Marangoni and buoyancy forces in the weld pool increase.
3. With increasing the laser power, increase in the weld pool depth is more than the half width. By increasing the welding current, the weld pool half width increases whereas the weld pool depth is relatively unchanged which is because the heat input from arc source is more concentrated on the weld surface. As well, by decreasing the welding speed, both the weld pool depth and half width increase with a similar slope.
4. Based on the statistical analysis of interaction effects, $I \times V_W$ interaction effect is more significant for the weld pool depth, while $P \times V_W$ interaction effect is more significant for the weld pool half width.
5. As a total conclusion, the presented numerical model showed a good capability to predict the weld pool shape and characteristics under various welding conditions when the welding parameters are not chosen out of the applied ranges, so that can reduce the number of needed experiments which causes time and money saving.

References

1. Bagger C, Olsen FO (2005) Review of laser hybrid welding. J Laser Appl 17(1):2–14
2. Mahrle A, Beyer E (2006) Hybrid laser beam welding—classification, characteristics, and applications. J Laser Appl 18(3):169–180
3. Ribic B, Rai R, DebRoy T (2008) Numerical simulation of heat transfer and fluid flow in GTA/Laser hybrid welding. Sci Technol Weld Join 13(8):683–693
4. Bendaoud I, Matteï S, Cicala E, Tomashchuk I, Andrzejewski H, Sallamand P, Mathieu A, Bouchaud F (2014) The numerical simulation of heat transfer during a hybrid laser–MIG welding using equivalent heat source approach. Optics Laser Technol 56:334–342
5. Ascari A, Fortunato A, Orazi L, Campana G (2012) The influence of process parameters on porosity formation in hybrid LASER-GMA welding of AA6082 aluminum alloy. Optics Laser Technol 44(5):1485–1490
6. Piekarska W, Kubiak M (2013) Modeling of thermal phenomena in single laser beam and laser-arc hybrid welding processes using projection method. Appl Math Model 37(4):2051–2062
7. Kong F, Kovacevic R (2010) 3D finite element modeling of the thermally induced residual stress in the hybrid laser/arc welding of lap joint. J Mater Process Technol 210(6–7):941–950
8. Brandizzi M, Satriano AA, Sorgente D, Tricarico L (2013) Laser–arc hybrid welding of Ti6Al4V titanium alloy: mechanical characterization of joints and gap tolerance. Weld Int 27(2):113–120
9. Moradi M, Ghoreishi M, Frostevarg J, Kaplan AFH (2013) An investigation on stability of laser hybrid arc welding. Opt Lasers Eng 51(4):481–487
10. Zhang C, Li G, Gao M, Yan J, Zeng XY (2013) Microstructure and process characterization of laser-cold metal transfer hybrid welding of AA6061 aluminum alloy. Int J Adv Manuf Technol 68(5–8):1253–1260
11. Chen YB, Lei ZL, Li LQ, Wu L (2006) Experimental study on welding characteristics of CO2 laser TIG hybrid welding process. Sci Technol Weld Join 11(4):403–411
12. Möller F, Thomy C (2013) Interaction effects between laser beam and plasma arc in hybrid welding of aluminum. Phys Procedia 41:81–89
13. Piekarska W, Kubiak M (2011) Three-dimensional model for numerical analysis of thermal phenomena in laser–arc hybrid welding process. Int J Heat Mass Transf 54(23–24):4966–4974
14. Ribic B, Palmer TA, DebRoy T (2009) Problems and issues in laser-arc hybrid welding. Int Mater Rev 54(4):223–244
15. Ming G, Xiaoyan Z, Qianwu H (2007) Effects of gas shielding parameters on weld penetration of CO2 laser-TIG hybrid welding. J Mater Process Technol 184(1–3):177–183
16. Tani G, Campana G, Fortunato A, Ascari A (2007) The influence of shielding gas in hybrid LASER–MIG welding. Appl Surf Sci 253(19):8050–8053
17. Liu LM, Yuan ST, Li CB (2012) Effect of relative location of laser beam and TIG arc in different hybrid welding modes. Sci Technol Weld Join 17(6):441–446
18. Xu GX, Wu C, Qin GL, Wang XY, Lin SY (2011) Adaptive volumetric heat source models for laser beam and laser+pulsed GMAW hybrid welding processes. Int J Adv Manuf Technol 57(1–4):245–255
19. Mazar Atabaki M, Nikodinovski M, Chenier P, Ma J, Liu W, Kovacevic R (2014) Experimental and numerical investigations of hybrid laser arc welding of aluminum alloys in the thick T-joint configuration. Optics Laser Technol 59:68–92
20. Faraji A, Goodarzi M, Seyedein S, Zamani M (2014) Experimental study and numerical modeling of arc and weld pool in stationary GTA welding of pure aluminum. Int J Adv Manuf Technol:1–13

21. Faraji AH, Bahmani A, Goodarzi M, Seyedein SH, Shbani MO (2014) Numerical and experimental investigations of weld pool geometry in GTA welding of pure aluminum. J Cent South Univ 21:20–26

22. Goodarzi M, Choo R, Takasu T, Toguri JM (1998) The effect of the cathode tip angle on the gas tungsten arc welding arc and weld pool: II. The mathematical model for the weld pool. J Phys D Appl Phys 31(5):569–583

23. Rai R, Elmer JW, Palmer TA, DebRoy T (2007) Heat transfer and fluid flow during keyhole mode laser welding of tantalum, Ti–6Al–4V, 304L stainless steel and vanadium. J Phys D Appl Phys 40(18): 5753–5766

24. Abderrazak K, Kriaa W, Ben Salem W, Mhiri H, Lepalec G, Autric M (2009) Numerical and experimental studies of molten pool formation during an interaction of a pulse laser (Nd:YAG) with a magnesium alloy. Optics Laser Technol 41(4):470–480

25. Faraji A, Goodarzi M, Seyedein S, Barbieri G, Maletta C (2014) Numerical modeling of heat transfer and fluid flow in hybrid laser–TIG welding of aluminum alloy AA6082. Int J Adv Manuf Technol:1–16.

26. Farzadi A, Serajzadeh S, Kokabi AH (2008) Modeling of heat transfer and fluid flow during gas tungsten arc welding of commercial pure aluminum. Int J Adv Manuf Technol 38(3–4):258–267

27. Farzadi A, Serajzadeh S, Kokabi AH (2010) Investigation of weld pool in aluminum alloys: geometry and solidification microstructure. Int J Therm Sci 49(5):809–819

28. Abderrazak K, Bannour S, Mhiri H, Lepalec G, Autric M (2009) Numerical and experimental study of molten pool formation during continuous laser welding of AZ91 magnesium alloy. Comput Mater Sci 44(3):858–866

29. Piekarska W, Kubiak M, Bokota A (2011) Numerical simulation of thermal phenomena and phase transformations in laser-arc hybrid welding joints. Archieve Metall Mater 56(2):409–421

30. Xu P-q, Bao C-m, Lu F-g, Ma C-w, He J-p, H-c C, Yang S-l (2011) Numerical simulation of laser–tungsten inert arc deep penetration welding between WC–Co cemented carbide and invar alloys. Int J Adv Manuf Technol 53(9–12):1049–1062

31. Hu B, Gd O (2005) Synergetic effects of hybrid laser/arc welding. Sci Technol Weld Join 10(4):427–431

32. Hu B, Gd O (2005) Laser induced stabilisation of the welding arc. Sci Technol Weld Join 10(1):76–81

33. Le Guen E, Carin M, Fabbro R, Coste F, Le Masson P (2011) 3D heat transfer model of hybrid laser Nd:Yag-MAG welding of S355 steel and experimental validation. Int J Heat Mass Transf 54(7–8): 1313–1322

34. Akbari M, Saedodin S, Toghraie D, Shoja-Razavi R, Kowsari F (2014) Experimental and numerical investigation of temperature distribution and melt pool geometry during pulsed laser welding of Ti6Al4V alloy. Optics Laser Technol 59:52–59

35. Rai R, Roy GG, DebRoy T (2007) A computationally efficient model of convective heat transfer and solidification characteristics during keyhole mode laser welding. Journal of Applied Physics 101 (5).

36. Roy GG, Elmer JW, DebRoy T (2006) Mathematical modeling of heat transfer, fluid flow, and solidification during linear welding with a pulsed laser beam. Journal of Applied Physics 100 (3).

37. Rai R, Kelly SM, Martukanitz RP, DebRoy T (2008) A convective heat-transfer model for partial and full penetration keyhole mode laser welding of a structural steel. Metall and Mat Trans A 39(1): 98–112

38. Dong H, Gao H, Wu L (2005) Heat transfer and fluid flow in fusion type PA-GTA double-sided welding. Model Simul Mater Sci Eng 13(8):1205

39. Yuzhen Z, Heping Z, Yaowu S (2006) The study of surface active element on weld pool development in A-TIG welding. Model Simul Mater Sci Eng 14(3):331

40. Zhou J, Tsai HL (2008) Modeling of transport phenomena in hybrid laser-MIG keyhole welding. Int J Heat Mass Transf 51(17–18): 4353–4366

41. Cho W-I, Na S-J, Thomy C, Vollertsen F (2012) Numerical simulation of molten pool dynamics in high power disk laser welding. J Mater Process Technol 212(1):262–275

42. Cho JH, Na SJ (2009) Three-dimensional analysis of molten pool in GMA-laser hybrid welding. Welding J (Miami, Fla) 88(2):35s–43s

43. Han S-W, Cho W-I, Na S-J, Kim C-H (2013) Influence of driving forces on weld pool dynamics in GTA and laser welding. Weld World 57(2):257–264

44. Jamshidi Aval H, Farzadi A, Serajzadeh S, Kokabi AH (2009) Theoretical and experimental study of microstructures and weld pool geometry during GTAW of 304 stainless steel. Int J Adv Manuf Technol 42(11–12):1043–1051

45. Gao Z, Ojo OA (2012) Modeling analysis of hybrid laser-arc welding of single-crystal nickel-base superalloys. Acta Mater 60(6–7):3153–3167

46. Haiyan Z, Wenchong N, Bin Z, Yongping L, Masaru K, Takashi I (2011) Modelling of keyhole dynamics and porosity formation considering the adaptive keyhole shape and three-phase coupling during deep-penetration laser welding. J Phys D Appl Phys 44(48): 485302

47. Ribic B (2011) Modeling of plasma and thermo-fluid transport in hybrid welding. The Pennsylvania State University, United States

48. Tsai NS, Eagar TW (1985) Distribution of the heat and current fluxes in gas tungsten arcs. Metall Trans B 16(4):841–846

49. Wu CS, Gao JQ (2002) Analysis of the heat flux distribution at the anode of a TIG welding arc. Comput Mater Sci 24(3):323–327

50. Ono M, Shinbo Y, Yoshitake A, Ohmura M (2002) Development of laser-arc hybrid welding. NKK TECHNICAL REVIEW 86:8–12

51. Zhang W, Kim CH, DebRoy T (2004) Heat and fluid flow in complex joints during gas metal arc welding-Part II: Application to fillet welding of mild steel. J Appl Phys 95(9):5220–5229